CrossMark

ORIGINAL ARTICLE

Earthquake dynamics on circular faults: a review 1970–2015

Raul Madariaga · Sergio Ruiz

Abstract We review the development of earthquake dynamics taken from the point of view of the origin of seismic radiation instead of the detailed study of rupture propagation on complex surfaces. Many features of seismic radiation can be explained by simple models that serve as elementary canonical problems. Some of these properties are very well known like the fact that at low frequencies, the seismic spectrum is proportional to the seismic moment. At high frequencies, on the other hand, radiation is generated by the motion of the rupture front, in particular stopping phases and geometrical obstacles (barriers). A rupture front moving at constant speed does not produce far-field radiation. For many practical applications, for determining source size and stress drop, for example, it is not necessary to determine geometrical details of the rupture. For such cases, a simple circular crack model is quite sufficient. An improvement on this method is to do dynamic inversion on simple, elliptical-shaped sources and letting the rupture start arbitrarily from a point on the fault. This problem can be solved nowadays with finite differences and a variety of inversion techniques.

R. Madariaga (✉)
Laboratoire de Geologie, UMR8538 CNRS Ecole Normale Superieure, Paris, France
e-mail: madariag@geologie.ens.fr

S. Ruiz
Departamento de Geofísica, Facultad de Ciencias Físicas y Matemáticas, Universidad de Chile, Santiago, Chile

1 Introduction

The first attempts to formulate a finite-source model compatible with mechanics and seismic observations started in the early 1960s with the rectangular kinematic dislocation models studied, for instance, by Haskell (1964), Ben-Menahem (1962) or Ben-Menahem and Harkrider (1964). In dislocation models, the propagation of rupture is fixed a priori and the slip distribution is determined by inversion. Kinematic models do not necessarily satisfy physical constraints on the propagation of shear fracture in the Earth. Dynamic source models on the other hand are based on fracture dynamics. They were introduced almost at the same time as kinematic models thanks to the concomitant development of theory and observations. Although there were many other fundamental contributions, we retain the following four: (1) development of fracture dynamics by Kostrov (1964, 1966, 1975) followed soon by work by Freund (1972a,b), Burridge and Halliday (1977), and many others. These authors provided the basic framework for the generation of seismic waves by shear faulting; they computed energy balance and introduced the new concept of dynamic energy release rate. Energy release rate had been introduced by Griffith (1921) for quasi-static fracture mechanics and Rice (1968) who showed that energy release rate was path independent. (2) In the early 1970s, the connection between fracture and friction was introduced by Ida (1972) for antiplane dynamic cracks based on Kostrov's (1966) solution for cracks moving at variable sub-shear speeds and by Palmer and Rice (1973) for quasi static shear slip. (3) Aki (1967)

introduced the concept of seismic source scaling and some basic properties of earthquake spectra that explained why magnitude scales gave different results at different frequencies. (4) Finally, Brune (1970) introduced the properties of seismic radiation, the so-called omega-squared model which was based on empirical observations and a simple radiation model.

Madariaga (1976, 1977) connected theory and observation producing a simple mechanical model of a circular seismic source that explained different observations already available at the time with more general fracture mechanical concepts. It turned out that the seismic spectra proposed by Aki (1967) and Brune (1970) could be explained by some general properties of earthquake dynamics. Similar results were obtained by Sato and Hirasawa (1973) who studied a circular fault that stopped abruptly at some finite time. The circular crack model provided a way to compute the scaling of corner frequencies with the size of the fault. Most practical work for finite-source modeling and inversion is still done using dislocation source models initially introduced by Haskell (1964, 1966). As shown by many authors (see, e.g., Madariaga 1977) dislocation models do not produce a finite energy radiation at high frequencies and therefore, they need to be regularized near the rupture front. The regularization is earthquake dynamics. Given that the main source of seismic observations is geodesy and seismic waves, earthquake source theory must be intimately related to seismic wave radiation. But this is very difficult to establish because earthquake rupture propagation is a very non-linear problem. Geophysicists linearise it by using dislocation sources moving at constant or slowly varying speeds that are then converted into dynamic models by a posteriori methods introduced by Fukuyama and Mikumo (1993), Bouchon (1997), and Ide and Takeo (1997). More recently, as will be discussed later in this paper, dynamic inversion has become possible for some particular earthquakes, but it is still far from being a standard procedure (Peyrat and Olsen 2004; Di Carli et al. 2010; Ruiz and Madariaga 2011, 2013; Diaz-Mojica et al. 2014; Twardzik et al. 2014). In spite of much progress in kinematics and dynamics, most kinematic and dynamic models explain the seismic spectrum up to frequencies of the order of 1 Hz or less. Modeling higher frequencies remains difficult because seismic wave propagation at higher frequencies requires detailed models of the structure of the earth and better and more detailed models of the rupture processes on the fault.

In this paper, we will briefly review some of the basic concepts that led to the classical fracture model of earthquakes, the circular shear crack, and recent attempts to do dynamic inversion.

2 The circular fault Model

2.1 The circular shear crack model

The circular shear crack model introduced by Kostrov (1964 and 1966) is considered as the first attempt to build a model of an earthquake source based on the then new concepts of fracture dynamics. The initial work on the corresponding static shear fault model was done by Eshelby (1957) and Keylis-Borok (1959). Let us consider the problem of a circular fault of radius a. Shear stress far from the fault has a constant value σ_0 and is zero inside the fault. Under these conditions, a solution for the slip on the fault ($r < a$) for Poisson ratio 0.25, can be written as

$$\Delta u(r) = \frac{24}{7\pi} \frac{\Delta\sigma}{\mu} \sqrt{a^2 - r^2} \qquad (1)$$

where r is the radius and $\Delta\sigma$ is the stress drop. For the circular crack model, the seismic moment in terms of the stress drop is given by

$$M_0 = \mu \Delta\overline{u} S = \frac{16}{7} \Delta\sigma a^3 \qquad (2)$$

The slip distribution (1) applies also to situations in which stress inside the fault does not drop to zero during slip. This occurs when faulting occurs under friction, the most common situation in earthquake dynamics. In this case, stress drop is the difference between the initial stress (σ_0) and the final stress (σ_f) under friction.

The stress outside the circular fault ($r > a$) can be computed using the method proposed by Eshelby (1959). The stress field around a circular crack is not cylindrically symmetric about the axis of the fault. The reason is that under shear, the crack is in fracture mode II in the direction of application of stress and in mode III in the direction transverse to the initial stress. Letting the initial stress be oriented along the x-axis and the normal to the fault being the z-axis, the stress field of the circular crack presents singularities of the inverse-square root type along the circumference of the crack. In cylindrical coordinates $(r,)$ on the plane of the fault, where r is the

radius from the origin of rupture and   is the azimuth measured from the mode II slip direction, we get

$$\sigma_{xz}(r,\phi) \approx (K_{II}\cos\phi + K_{III}\sin\phi)\frac{1}{\sqrt{2\pi}}\frac{1}{\sqrt{r-a}} \qquad \text{for} \quad r > a \tag{3}$$

and a similar expression applies for the other shear stress component on the fault, σ_{yz}. Here, K_{II} and K_{III} are the in-plane and antiplane stress-intensity factors, respectively. Thus, stresses are square root singular around the fault with an intensity that depends on the two coefficients

$$K_{II} = \frac{16}{7\sqrt{\pi}}\frac{1}{1-\nu}\Delta\sigma\, a^{1/2} \qquad \text{and} \qquad K_{III} = \frac{16}{7\sqrt{\pi}}\Delta\sigma\, a^{1/2}$$

where ν is the Poisson's modulus, $\Delta\sigma$ is the stress drop assumed constant inside the fault, and a is the fault radius. For the usual value $\nu = \frac{1}{4}$ used in seismology, the mode II stress-intensity factor is four thirds times the mode III intensity factor. In summary, slip is maximum at the center of the fault and has an ellipsoidal shape that decreases to zero near the edges of the fault. Associated with this decrease in slip, inverse-square root singularities appear at the edge of the fault ($r = a$).

2.2 Circular fault. Brune's model

The most common model for a circular fault of finite dimensions was proposed by Brune (1970, 1971). Brune derived this model from the assumption that faulting occurred instantaneously on a flat circular shear crack. From several energy conservation arguments he proposed that the far-field displacement of S waves at distance r from the fault was of the form

$$u(t) = \frac{1}{4\pi\rho\beta^3}\frac{1}{r}R^S M_0\omega_c^2 \ \ \beta\left(t-\frac{r}{\beta}\right)e^{-\omega_c\left(t-\frac{r}{\beta}\right)} \ \ H\left(t-\frac{r}{\beta}\right) \tag{4}$$

where R^S is the S wave radiation pattern and ρ and β are the density and shear wave velocity of the elastic medium, respectively. H is Heaviside's distribution. In Eq. 4, ω_c is the corner frequency. The amplitude of the Fourier spectrum of $u(t)$ is given by,

$$\left|U(\omega)\right| = \frac{1}{4\pi\rho\beta^3}\frac{1}{r}R^S M_0\frac{1}{1+\omega^2/\omega_c^2} \tag{5}$$

This Fourier spectrum has the usual form of Brune's inverse ω squared model. It is flat at low frequencies less

than the corner frequency ω_c and decays like the inverse square of the frequency ω at high frequencies. From an argument about the conservation of high-frequency energy, Brune proposed that the corner frequency was related to the fault radius by

$$\omega_c = 2.34\frac{\beta}{a} \tag{6}$$

The corner frequency ω_c is inversely proportional to the source radius a. This relation is widely used in seismology and earthquake engineering to determine the radius of the fault from the corner frequency of the spectrum of S waves. It should be noted that the radiation from an instantaneous circular shear crack is not of the form (Eqs. 4 and 5) and that the actual high-frequency decay of the spectrum (Eq. 5) is of the order of $\omega^{-5/2}$, i.e., faster than ω^{-2}, as shown by Madariaga (1976).

2.3 Energy balance for Brune's circular model

A very important and still poorly understood issue in seismology is the energy balance of earthquakes. The circular crack model has the very useful property that all relevant energies can be computed exactly. For a circular crack, the static slip produces a total strain energy release that can be directly computed from the slip distribution (Eq. 1):

$$\Delta W = \int_S \overline{\sigma}\Delta u \ dS \tag{7}$$

where $\overline{\sigma} = 1/2\ (\sigma_0 + \sigma_f)$ is the average stress acting on the fault. This energy is actually dissipated in two ways: first as friction (mostly heat) that is equal to

$$\Delta T = \int_S \sigma_f\Delta u \ dS \tag{8}$$

and as the available elastic energy ΔU, the energy that is available to produce seismic radiation and to make rupture grow:

$$\Delta U = \frac{1}{2}\int_S \Delta\sigma\Delta u \ dS \tag{9}$$

with $\Delta W = \Delta U + \Delta T$. In a circular crack, the available strain energy can be directly computed from the slip

distribution (Eq. 1) since $\Delta\sigma = \sigma_0 - \sigma_f$ is assumed to be constant, so that

$$\Delta U = \frac{8}{7}\frac{\Delta\sigma^2}{\mu}a^3 \qquad (10)$$

We can now compare the available energy (Eq. 10) with the seismic energy actually radiated by Brune's model. This can be computed from the expression for the energy radiated by a point source (Eq. 4.87 of Udias et al. 2013):

$$E_s = \frac{1}{4\pi^2\rho}\left(\frac{1}{\alpha^5}\langle R_P^2\rangle + \frac{1}{\beta^5}\langle R_S^2\rangle\right)\int_{-0}^{\infty}\omega^2\left|M_0(\omega)\right|^2 d\omega$$

for S waves, we get

$$E_s = \frac{1}{16\pi\mu}\langle R_S^2\rangle M_0^2\frac{\omega_c^3}{\beta^3} = \frac{2.34}{7}4\langle R_S^2\rangle\frac{\Delta\sigma^2}{\mu}a^3$$

where we wrote M_0 and ω_c in terms of stress drop $\Delta\sigma$ and the radius of the fault a. Finally, we use the root mean squared averaged radiation pattern $\langle R_S^2\rangle = 0.4$ to find

$$E_s = 0.535\frac{\Delta\sigma^2}{\mu}a^3 = 0.47\Delta U \qquad (11)$$

The value of 0.47 for the ratio between E_s and ΔU was assumed by Brune (1970, Eq. 39). Defining the radiation efficiency (Husseini and Randall 1976) as $\eta_r = E_s/\Delta U$, Brune's model has an efficiency of 47 %. This about half the maximum possible radiated energy. Where does the rest of the available energy go? It goes into fracture energy, the energy that is used to create the fault surface. This could not be clearly explained in Brune's (1970) model because he assumed that the fault broke instantaneously at time $t = 0$.

2.4 Scaling laws

Earthquakes occur with very different sizes from very small ones that can only be detected by extremely sensitive instruments to very large ones that produce catastrophic damage and ground rupture along hundreds of kilometers. It is possible to establish scaling laws among the parameters that control seismic rupture, so that some parameters can be expressed in terms of some other more fundamental ones (Madariaga and Olsen 2002). The first seismic scaling law was introduced by Aki (1967) from considerations about the different magnitude scales that were in common use at

the time. His argument was that all these magnitude scales could be reconciled if all earthquakes shared the seismic wave spectrum with a flat part at low frequencies and with ω^{-2} decay of amplitude at high frequencies, just like the Brune model of expression (5). He then compared the spectrum of earthquakes of different sizes and concluded that the corner frequency was inversely proportional to the size of the earthquake, and that the moment was proportional to the stress drop times the cube of the source length and times the inverse of the cube of the corner frequency, that is:

$$M_0 \approx \Delta\sigma a^3 \approx \Delta\sigma\omega_c^{-3} \qquad (12)$$

Comparing earthquakes of different size occurring in similar tectonic areas, he found that the scaling relation implied that within an order of magnitude, stress drop $\Delta\sigma$ was essentially the same for all earthquakes. It has been observed by Kanamori and Anderson (1975) and Hanks (1977) that most earthquakes have fairly constant stress drops between 0.1 and 10 MPa. In Fig. 1, we show a collection of observations of moment and length of many earthquakes, in many different environments including very recent events of large magnitude (from Zollo and Emolo 2011). It is observed that the ensemble of observations fills a region between two lines that correspond to stress drops of 1 to 10 MPa for an equivalent circular fault. The moments reported in Fig. 1 stretch over 10 orders of magnitudes.

2.5 Energy scaling

If we follow the circular shear crack model, we observe that strain energy change during an earthquake scales like $\Delta U \sim \Delta\sigma^2 a^3$ (see Eq. 10); while moment scales like $M_0 \sim \Delta\sigma a^3$ (Eq. 3). Thus, two quantities that have the same dimensions ($J = Nm$) scale differently, one like $\Delta\sigma$ the other like $\Delta\sigma^2$. We can now recall relation (Eq. 11) according to which radiated energy also scales like $E_s \sim \Delta\sigma^2 a^3$. It is clear that the circular crack model has additional features that were not taken into account in the instantaneous crack model of Brune. These differences between the scaling energy and moment with stress drop are not always obvious because very often, it is assumed that $\Delta\sigma$ is the same for all earthquakes. We can finally produce an alternative scaling law between energy and moment for Brune's model based on the

Fig. 1 Relation between seismic moment, magnitude M_w, and fault length for earthquakes with a broad range of magnitudes. The *gray zone* is the area where most earthquakes lie. The *dots* are significant recent earthquakes
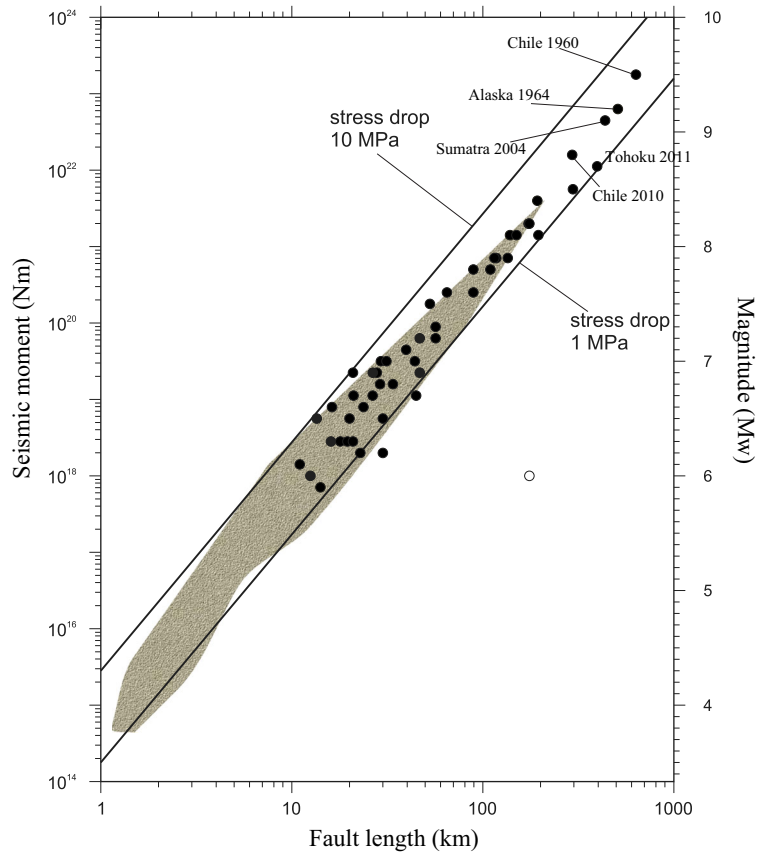
relationship (Eq. 11) where we replace the radius a by its expression (Eq. 6) in terms of the corner frequency:

$$E_s = 0.00796 \frac{M_0^2}{\mu} \frac{\omega_c^3}{\beta^3} = 1.9739 \frac{M_0^2}{\mu} \frac{f_c^3}{\beta^3} \qquad (13)$$

Where $\omega_c = 2\pi f_c$. This relationship can be used to test whether Brune's model applies to a particular earthquake or to a suite of seismic events. In general, we should expect that the coefficient in Eq. 13 depends on the rupture process, average rupture speed, friction law, etc. (see, e.g., Ide and Beroza 2001; Abercombrie and Rice 2005; Lancieri et al. 2012). We notice that although the numerical coefficient in Eq. 13 was computed for Brune's model, it can be computed for any kinematic or dynamic model of seismic radiation. Expression 13 also shows that radiated energy is not proportional to moment but to moment squared.

3 Rupture of a quasi dynamic circular fault

As already mentioned earlier, Brune (1970) assumed that rupture occurred instantaneously across the fault so that the process of fracture propagation was not modeled. A more realistic model for a circular earthquake source is a shear fault that expands at subsonic velocity v under constant stress conditions (Madariaga 1976). We call quasi-dynamic model one with imposed rupture speed but well-defined stress drop. In more advanced earthquake models, discussed in the following sections, the rupture velocity will be allowed to change as the crack propagates. For many earthquakes, however, the circular crack propagating at constant speed provides a sufficiently simple model that can be used to compute its most fundamental properties, like size, stress drop, etc.

We consider a circular rupture embedded in an infinite homogeneous isotropic elastic medium where a circular crack expands from the origin at constant rupture velocity. Although this very simple problem has no exact solution, it can be solved numerically by a finite

difference method. At the time when this model was first studied, computer resources were very limited so that several simplifying assumptions were made. One of them was that as the crack was expanding slip on the fault was everywhere parallel to the applied stress. Although we know that this approximation is not entirely correct, modern studies have shown that the assumption was reasonable (Bizzarri and Cocco 2003). If slip on the fault is everywhere parallel to a coordinate axis, the problem can be reduced to a cylindrical one and solved numerically with a specific technique. Nowadays, it is just as simple to use a straightforward cubic grid as proposed by Madariaga et al. (1998) for finite differences.

Since we are assuming that the material properties and the initial stress field are homogeneous, once the rupture begins to propagate it would continue to propagate without limit. If we want the fracture to come to a stop, when the radius takes a particular value a, we have to impose this as a boundary condition, that is, motion stops at $r = a$ when $t = a/v$. Let the fault plane be on the plane $x_3 = 0$, and shear stress act in the x_1 direction ($\sigma_{13} = \sigma_0$). Before rupture initiation ($t < 0$), the fault is subjected to a uniform state of stress at large distances from the fault. At $t = 0$, the shear stress acting on the fault is considered to be sufficient to initiate rupture. Before rupture stops, we can solve for the slip rate inside the fault exactly using the self-similar slip distribution found by Kostrov (1964). Slip inside the fault before the rupture stops is given by

$$\Delta u = C(v) \frac{\Delta \sigma_d}{\mu} \sqrt{(vt)^2 - r^2} \quad \text{for } r < vt \qquad (14)$$

Where $C(v)$ as a constant that depends on the rupture speed. Actually, $C(v)$ is very close to one for the entire rupture velocity range from 0 to the Rayleigh wave speed. According to Madariaga (1976), $C(v) = 1$ for $v = 0$, and $C(v) = 0.9$ when v approaches the Rayleigh wave speed. Taking the derivative with respect to time, the slip velocity can be written for constant $\Delta \sigma_d$ as

$$\Delta \dot{u} = C(v) \frac{\Delta \sigma_d}{\mu} \frac{v^2 t}{\sqrt{(vt)^2 - r^2}} \quad \text{for } r < vt \qquad (15)$$

which shows that as in all crack models, the slip velocity field has an inverse-square root singularity right behind the propagating rupture front ($r = vt$).

In Fig. 2, we show the numerical solution for slip as a function of position and time obtained for a circular crack that propagates at 80 % of the shear wave speed. The elastic medium has a P wave speed of 6200 m/s, shear wave speed of 3520 m/s, and density is 2700 kg/m^3; thus, the rupture speed is $v = 2534$ m/s. We assumed that kinematic (or effective) stress drop $\Delta \sigma_d$ was 4 MPa. As observed in the figure, once the rupture reaches the

Fig. 2 Numerical solution for the slip as a function of position and time for a quasi-dynamic circular fracture propagating at 80 % of the shear wave speed. The most remarkable healing phases that propagate from the border of the circle toward the center, P, and Rayleigh wave velocities
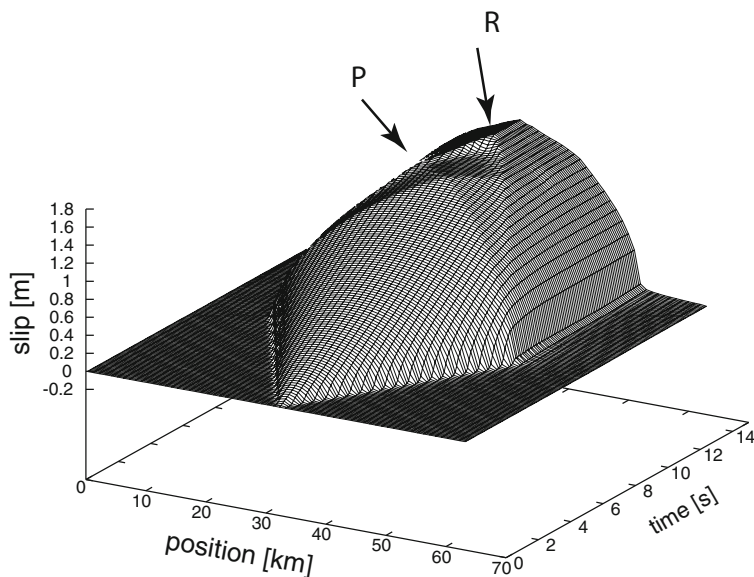
final radius of $a = 20$ km, it stops growing instantaneously. This generates three healing phases that propagate inward from the edge of the crack with velocities α, β, and the Rayleigh wave speed c_R. The slip distribution in Fig. 2 is plotted along the longitudinal (mode II) axis. A very similar distribution can be plotted along the transverse (mode III) axis; differences appear only after the arrival of P healing phase because along the mode III axis, P wave is very weak, almost null. Thus, even for this very simple model, slip distribution is not cylindrically symmetric on the fault plane once the rupture front interacts with the borders of the fault. Our numerical calculation takes into account these asymmetries.

Once the healing phases reach the center of the fault, slip reduces rapidly and it ceases completely after the Rayleigh waves have crossed each other. This healing occurs because after the Rayleigh wave, slip rate becomes negative reversing the sense of friction. The final slip on the fault after the rupture stops can be approximated by the static solution for a circular crack (Eq. 1). Although the final slip computed numerically with high resolution is not exactly of the elliptical shape predicted by the static solution (Eq. 1), the elliptical distribution is a good approximation for many purposes. Computations for many simulations at different speed show that the static stress drop $\Delta\sigma_s$ is always larger than the dynamic stress drop $\Delta\sigma_d$ for the circular shear crack. For instance, for a crack running at $v = 0.9\beta$, Madariaga (1976) found that $\Delta\sigma_s = 1.2\Delta\sigma_{d.}$. For the example shown in Fig. 2, the final static stress drop is not uniform but is still about 15 % higher than the kinematic stress drop (effective stress in Brune's terms). Finally, we can compute the seismic moment released by the circular crack model of Fig. 2, it is $M_0 = 4.9 \times 10^{19}$ Nm, which is equivalent to a moment magnitude $M_w = 7.0$.

3.1 Energy balance of the quasi-dynamic circular shear fault

We mentioned that Brune (1970) made a crude approximation to the radiation from a circular shear crack by equating the high-frequency energy flow in the direction perpendicular to the fault to that observed in the far field. The self-similar circular crack model provides a simple way to compute the energy balance. For that purpose, we use the model of Kostrov (1964) growing at constant speed v from an initial point as was assumed in the initial part of our numerical solution shown in Fig. 2. As

shown by Madariaga (1976) the total energy released by fracture growth, called E_F, is

$$E_F = 2\pi \int_0^a G_c(r, v)r\,dr$$

where $G_c(r,v)$ is the energy release rate computed for a self-similar circular crack growing at constant speed v. Omitting details E_F is:

$$E_F = \frac{\pi}{3} g(v) \frac{\Delta\sigma_d^2}{\mu} a^3 \tag{16}$$

Where $g(v)$ is smoothly varying function of rupture velocity that has a complex expression given by Madariaga (1976). A misprint in the original expression was corrected by Ide (2002). The rupture velocity-dependent factor $g(v)$ decreases monotonically from 1 at $v = 0$ to 0.1 at $v = 0.9\beta$. The most important feature of Eq. (16) is that the total energy spent in propagation of the circular rupture grows in proportion to the cube of the radius. $G_c(r)$, the specific energy release rate per unit surface of the fault, grows like the radius as the fault expands. Thus, G_c for a circular shear crack is *not a constant* but a function of radius. Recalling from Eq. 10 that the strain energy release by a circular crack also grows like the cube of the radius and so does the radiated energy (Eq. 11) we observe that all energy like quantities in the circular fault grow in proportion of radius to the cube and the square of the stress drop.

The most obvious consequence of the scaling of energy balance is that for a circular shear crack growing at constant rupture speed, the energy release rate *is not a material constant* as assumed in the Griffith model of fracture (see discussion by Abercombrie and Rice 2005 and Lancieri et al. 2012). Either faults do not propagate at constant rupture speed and adjust their speed to produce a constant energy release rate or, more likely, G_c is not a material property.

3.2 Far-field displacements of a dynamic circular fault

Up to this point, we have discussed the main features of the slip distribution produced by a propagating circular fault. Now, we will consider the relation between elastic wave radiation field and the dynamic process at the source. The far-field P or S wave displacement produced by the circular crack in a homogenous medium can be computed from the distribution of slip velocity
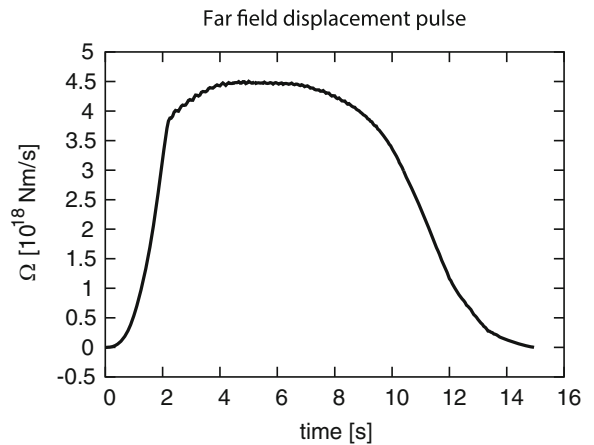
$\Delta u^{.}$. For the circular shear crack the far-field S waves are given by

$$u^{P,S}(r,\theta,\phi,t) = \frac{\mu}{4\pi\rho c^3}\frac{1}{r}R_c\int_{\Sigma}\Delta\dot{u}\left(r',\varphi,t-\frac{r}{c}+\frac{r'\sin\theta}{c}\right)dS'$$

(17)

where P,S indicate whether a P or an S wave is being modeled. c stands for the P or the S wave speed as a function of the wave being computed. r_i is the position vector from the origin to the observation point (r, θ, φ) with θ as the polar angle of the vector r_i measured from the vertical to the fault, φ is its azimuth, and r the position on the fault. R_c is the radiation pattern corresponding to a shear fault point source at the center of the fault, which we consider to be only a function of the location of the observation point $R_c(r, \theta, \varphi)$. A simple kinematic model for a circular crack was proposed by Sato and Hirasawa (1973) in which rupture initially followed the Kostrov (1964) slip distribution (Eq. 14) and then slip rate dropped to zero at some finite time. Such a model is the only one for which we know an analytical expression for the far-field radiation (see Udias et al. 2013, section 7, for a full discussion).

For all other dynamic models, the far-field radiation may be computed using Eq. 17. Its numerical evaluation poses no problem once the slip rate distribution $\Delta u^{.}$ has been computed. We are also very much interested in the spectrum of the radiated waves because most studies of earthquakes parameters are done using the spectrum. The spectrum of radiated waves can be computed by straightforward numerical Fourier transform of Eq. 17. We used Eq. 17 to compute the far-field radiation from the circular crack model shown in Fig. 2. We call Ω_0 the term under the integral in Eq. 17. We computed it for the angles $\theta = 60°$ and $\varphi = 0$ is shown in Fig. 3. The amplitude is given in units of moment rate for displacement, the duration of the signal is about 12 s, which is approximately twice the time for the rupture to cross the fault radius of 20 km at a rupture speed $v = 2534$ m/s.

In Fig. 4, we show the displacement spectrum for the shear waves. We can distinguish three parts in the far-field displacement spectrum. In the first part, corresponding to the low frequencies, the spectrum is flat with a value proportional to the seismic moment $M_0 = 4.9 \ 10^{19}$ Nm, as the fault appears as a point source. In the second part,


Far field displacement pulse

Fig. 3 Far-field radiation from a quasi-dynamic circular shear crack. Displacement pulse observed in the far field of a circular fault of 20-km radius and rupture velocity of 2.534 km/s

corresponding to the intermediate frequencies, the shape of the spectrum is controlled by the size of the fault. In this part, the envelope of the spectrum may have several decay rates, depending on the azimuth of the observation point. At high frequencies, beyond the corner, the spectrum decays like ω^{-2}. The high-frequency decay, inversely proportional to the square of the frequency, is controlled by the discontinuities of the seismic pulse, in particular by the stopping phases. As we see in Fig. 3, the most important stopping phase is observed at time $t_1 = 2$ s, near which the far-field displacement has an abrupt change. This is the first stopping phase coming from the edge of the fault closest to the observer. The second stopping phase, located at $t_2 = 11.5$ s, is less remarkable than the first one because it is emitted by the far edge of the fault so that directivity is weaker. This stopping phase suffers a phase shift (Hilbert transform) when it crosses the axis of the fault. More details were presented by Madariaga (1977) who found asymptotic approximations for these stopping phases.

The complicated shape of the spectrum shown in Fig. 4 depend on both θ and φ. This makes it difficult, in practice, to provide a single value of the corner frequency as a function of radius and rupture velocity. The corner frequency, as we have seen, is usually determined as the intersection of two straight lines fitted to the spectrum in the low and intermediate frequency parts. A general property of the amplitude spectra is that the corner

Fig. 4 Far-field spectrum of the shear waves radiated by a circular shear crack of radius 20 km and rupture velocity 2.534 km/s. This is the amplitude Fourier spectrum of the far-field displacement pulse of Fig. 3
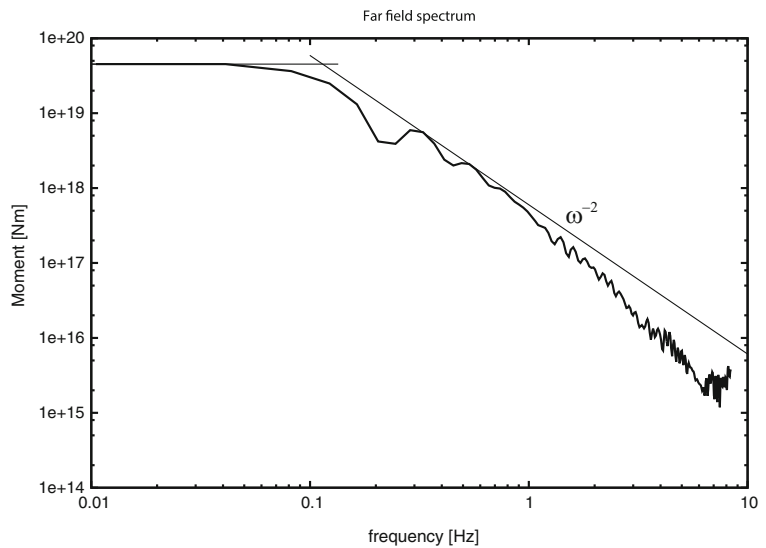
frequencies of P waves are higher than those of S waves. This reflects the fact that in the time domain, the S wave pulses are longer than those of P waves. For $v = 0.9\beta$ and $\alpha/\beta = 1.732$, the values for the corner frequencies of P and S waves are

$$\begin{aligned} \omega_c{}^P &= 1.16 \ \alpha/a \\ \omega_c{}^S &= 1.32 \ \beta/a \end{aligned} \tag{18}$$

A much more detailed study of quasi-dynamic and dynamic circular shear crack models was carried out by Kaneko and Shearer (2014, 2015) who computed corner frequencies for different rupture seeds and radiation angles (θ, φ).

4 A dynamic circular fault in a homogeneous medium

In this section we study the spontaneous propagation of rupture starting from an initial circular asperity and the arrest of rupture at an unbreakable circular barrier.

4.1 Friction

The problem of dynamic rupture is ill-posed if there is no friction law applied on the fault. The consequence of the lack of friction is that rupture is instantaneous or propagates at the P wave speed in mode II and the shear wave speed in mode III. For any causal control of rupture, we have to take into account friction on the fault plane, or alternatively, we have to introduce the

amount of energy spent in rupture growth, G_c defined earlier. The origin of G_c in friction laws was first studied by Ida (1972) who used slip weakening at high speeds. Similar results were derived for quasi-static crack growth by Palmer and Rice (1973).

Friction controls the initiation and propagation of rupture and the healing of faults. Because at high speeds, most friction laws are equivalent (see Bizzarri and Cocco 2003 and Daub and Carlson 2008), in the following, we will use the slip-weakening friction law, in which the slip is zero until the total stress reaches a peak value of static friction that we denote σ_s. Once this stress has been reached, the slip Δu starts and the friction decreases until it reaches a residual or kinematic friction σ_k:

$$\sigma(D) = \sigma_s - (\sigma_s - \sigma_k)^{\Delta u}/_{D_c} \qquad \text{for} \qquad \Delta u < D_c \tag{19}$$

where D_c is the slip-weakening distance and σ_s and σ_k are the static and kinematic friction, respectively. For $\Delta u > D_c$ the stress drop is total, so that $\sigma = \sigma_k$. This friction law has been extensively used in numerical simulations of rupture by Andrews (1976), Day (1982) and many others. Without loss of generality, and for simplicity of the numerical simulations, we will measure all stresses with respect to the kinematic friction σ_k. This is equivalent to assuming that $\sigma_k = 0$ in Eq. 19. It is an important property of linear dynamic ruptures that the slip, energy balance, and seismic radiation depend only on the stress change, not on the absolute stress levels. In other words, we can add to Eq. 19 any stress field that is in equilibrium with its sources because the seismic

waves generated by the fault ignore the presence of preexisting stresses in the elastic medium. Seismic waves only interact with preexisting stress in the fault zone or if wave propagation is non-linear. The most important feature of the friction law (Eq. 19) is that in order to propagate rupture along the fault plane, the elastic medium surrounding the fault has to provide a fracture energy per unit surface equal to the energy release rate, $G_c = \frac{1}{2}(\sigma_s - \sigma_k)D_c$.

4.2 Scaling of dynamic rupture

The equations of motion for elastic waves contain no intrinsic length or stress scales except for the size of possible elastic wave heterogeneities. For uniform elastic media, the stress and length scales are entirely determined by the boundary conditions and the initial stress field. From a dimensional analysis of the source problem in a uniform medium, we conclude that rupture propagation is completely controlled by the following physical and geometrical parameters:

1. The initial stress field σ_0;
2. The parameters D_c, σ_s, and σ_k, of the friction law (Eq. 19).
3. The length scales that define the geometry of the fault; in our case, the radius a.

Like any other non-linear problem in physics, the solutions of earthquake dynamics are controlled by a number of non-dimensional parameters, which can be defined from appropriate dimensional analysis of the equations and boundary conditions. For earthquake dynamics, there are two non-dimensional numbers, which have been well identified. These are the stress ratio (S), introduced by Das and Aki (1977),

$$S = \frac{\sigma_s - \sigma_0}{\sigma_0 - \sigma_k} \tag{20}$$

and the energy ratio (k) proposed by Madariaga and Olsen (2002)

$$\kappa = \frac{(\sigma_0 - \sigma_k)^2 a}{\mu(\sigma_s - \sigma_k)D_c} \tag{21}$$

The ratio S is closely related to the transition from sub- to super-shear rupture propagation, while κ controls the initiation of rupture and the overall qualitative nature of the rupture. It is possible to derive other parameters from

the equations of motion; for instance, the ratio of the overall dimension of the fault and the average fault slip, but they have not been discussed in the literature.

Let us study the spontaneous propagation of rupture on a flat fault. Rupture occurs under slip-weakening friction defined in Eq. 19. We use the same overall size as in the study of the quasi-dynamic circular fault. The space and time steps will also be the same: 200 m and 0.01 s, respectively, insuring that the Courant–Friedrichs–Lewy (CFL) constant that controls convergence of finite differences is $H = 0.178$. In order to obtain a circular rupture, we introduce an unbreakable barrier, concentric with the initial asperity, with radius 20 km. It would be interesting to study cases where the initial asperity or hypocenter is not located at the center of the circle (Kaneko and Shearer 2015). Since we are interested in comparing spontaneous rupture simulations with the quasi-dynamic circular crack model of the previous section, we use a stress drop of 4.5 MPa so that the rupture does not become super-shear in our simulation. Peak stress in the friction law was 8 MPa and D_c was 0.2 m so that energy release rate was 0.8 MJ. The non-dimensional parameter κ was 1.21. These parameters insure that rupture propagation is sub-shear in the in-plane direction. Snapshots of the slip rate are shown in Fig. 5 at several successive instants of time measured in seconds. We observe in Fig. 5 that after 1.7 s, the rupture becomes spontaneously elongated in the horizontal direction, which is also the direction of the initial stress. In this direction, mode II prevails. In the transverse (vertical) direction, the slip is in mode III. Thus, as already remarked by Das (1980) and Day (1982), the rupture tends to grow faster in the in-plane direction, which is dominated by mode II. At time $t = 6.5$ s, the rupture has reached the unbreakable border of the fault in the in-plane direction and is already healing in the in-plane direction. At time $t = 8.1$ s, the stopping phases generated by the edges of the fault are moving toward the center of the fault. The slipping patches in the darker regions are now elongated in the antiplane direction, owing to slower healing.

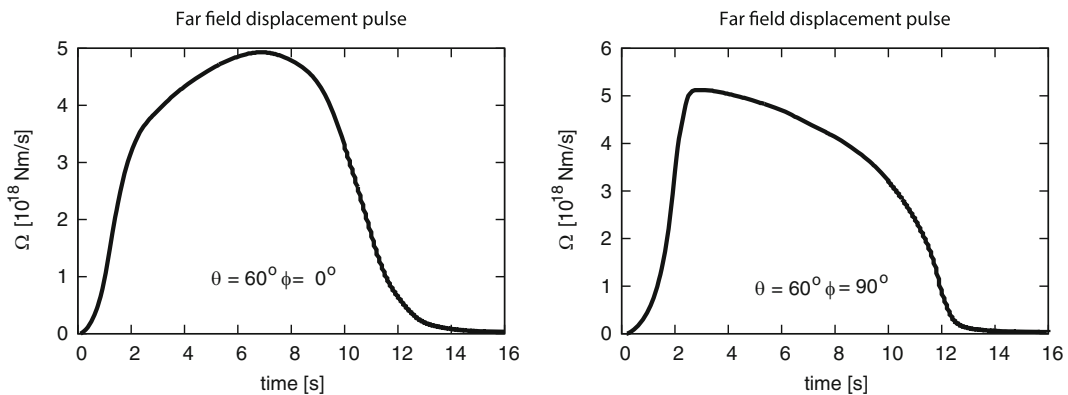## 4.3 Radiation from the spontaneous circular crack

How much does spontaneous rupture affect the quasi-dynamic circular crack models? To respond to this question, we computed the seismic radiation from the dynamic model. As for the quasi-dynamic model, there are significant differences in the seismic signal pulses

Fig. 5 Snapshots of the slip rate on a finite circular crack of 20-km radius with a fixed border. The *darker regions* show higher slip rates. The rupture propagation is sub-shear. The non-dimensional parameter values are $S = 0.78$ and $k = 1.71$. The rupture reaches the border at 6.1 and at 7.3 s the stopping phase propagates inwards
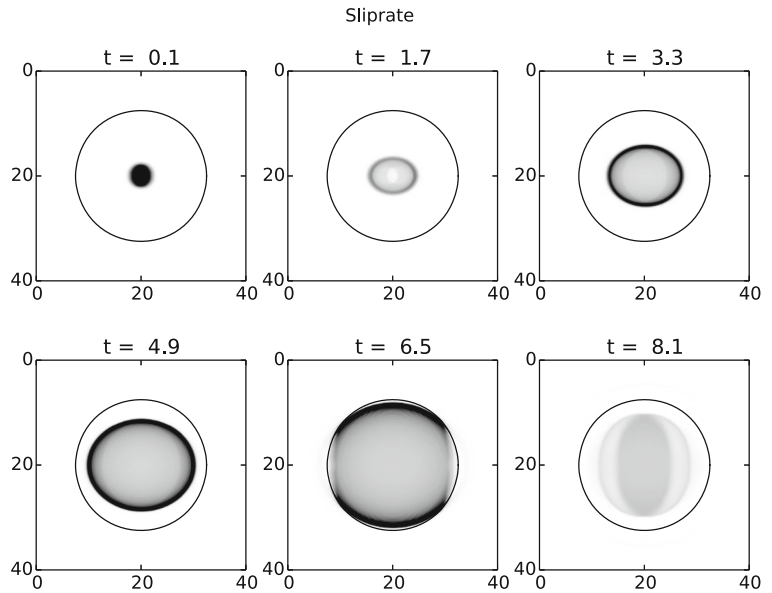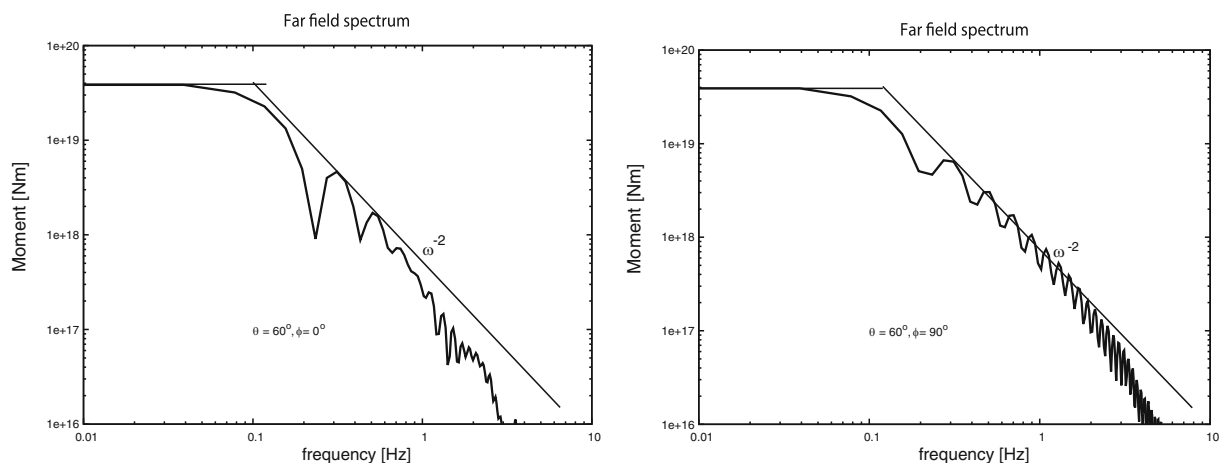

radiated in different directions of space. To illustrate this variability, we show in Fig. 6 the radiation in two directions of space: along the mode II direction and along the transverse or mode III direction. The angles θ and ϕ are the polar angles measured from the normal to the fault plane and the azimuth measured from the direction of slip on the fault. The displacement signals in two different directions ($\theta = 60°$, $\phi = 0°$ and $\theta = 60°$, $= 90°$) are shown in Fig. 6. Both have roughly the same duration, of about 10 s, but are quite different because one (for $= 90°$) has a larger displacement at the beginning of the signal while the other is stronger near the end. The reason is that the stopping phases, the abrupt changes in slope in the figures, have different

amplitudes. The corresponding amplitude spectra are shown in Fig. 7; these spectra have the typical ω^{-2} spectral decay at high frequencies. We can compare the signals of Fig. 6 with those emitted by the quasi-dynamic model, shown in Fig. 3. They are similar, but the size of the stopping phases is again different. The spectra of Figs. 3 and 6 are very similar: they have the same spectral shape and the corner frequencies vary from 0.1 to 0.12 Hz, the quasi-dynamic model having the highest corner frequency. It is not surprising that very different time-domain signals produce similar spectra. The reason is that the spectra are dominated by the stopping phases, which carry the information about rupture arrest. Although arrest is faster in the in-

Fig. 6 Radiation by the spontaneous circular fault of Fig. 5. Far-field displacement pulses are shown for two direction of space. $\theta = 60°$ is the polar angle measured from the fault normal and is the azimuth measured from the longitudinal (mode II) axis, the in-

plane direction. On the *left*, far-field pulse along the in-plane (mode II) direction. On the *right*, the far-field pulse radiated along the anti-plane (mode III) direction

Far field spectrum

Far field spectrum

spite of the difference in shape of the time-domain signals, the spectra have the same Brune (1970) spectral shape

plane direction, the difference in arrival time of the stopping phases is not very large, so that the main features of the spectrum are preserved. It is possible to study the variation in the corner frequency as a function of the polar or azimuth angles, but the effect of moving the initiation point with respect to the circular border is much more important (see Kaneko and Shearer 2014, 2015 for a full discussion).

5 Dynamic inversion

The first attempts at dynamic inversion were based on the conversion of source models obtained by kinematic inversion into dynamic models (Fukuyama and Mikumo 1993; Bouchon 1997; Ide and Takeo 1997). The first attempts at direct dynamic was the trial and error method used by Peyrat et al. (2001) to develop a dynamic rupture model of the Landers earthquake. This is a tedious but enlightening method for understanding rupture propagation starting from a kinematic slip model. In the present section, we introduce a dynamic non-linear inversion method where the best model is searched by exploration of a limited parameter field. This approach is non-linear because the seismic waves do not depend linearly on the parameters of the source model. However, if we can reduce the source model in such a way that it can be processed by a single node in a multicore machine, it is possible to run many different models in parallel. The first attempts at dynamic inversion were made by Peyrat and Olsen (2004), Corish

et al. (2007) and Di Carli et al. (2010), who inverted the Mw 6.7 Tottori 2000 earthquake in Japan. From these early experiences, it was clear that dynamic inversion was only feasible for relatively simple models. Di Carli et al. (2010) used an elliptical patch model proposed by Vallée and Bouchon (2004) to capture the long wavelength features of an inverted event.

5.1 Iwate earthquake of 2008

The 2008 Iwate $M_W = 7.1$ intraplate earthquake at 115-km depth was well recorded by the Japanese strong motion networks KiKnet and K-NET, as shown in Fig. 8 where the star shows the epicenter and the rectangles show the locations of the strong motion instruments used in the inversion. The gray and black circles show the sites that were used by Ruiz and Madariaga (2013) to do a second inversion to verify that the results are robust. The Iwate earthquake was studied in detail by Suzuki et al. (2009), who proposed two different kinematic source models. One using a couple of intersecting fault planes and another that uses a single fault. For dynamic inversion, we adopted the single fault plane model shown in Fig. 8 (strike 178°, dip 73°, and rake −95°). For dynamic inversion, we used a single elliptically shaped fault model instead of the usual grid of rectangles in kinematic inversions. The stress and friction were uniform inside the elliptical fault patch. Rupture propagation was controlled by the slip-weakening friction law (Eq. 19). For simplicity, in the following, we will assume that the residual friction

Fig. 8 Dynamic inversion of the M_w 7.1 Iwate intermediate-depth earthquake of 24 July 2008. The *rectangles* show the stations used for the inversion and the *circles* show the stations used by Ruiz and Madariaga (2013) for the verification of the inversion results
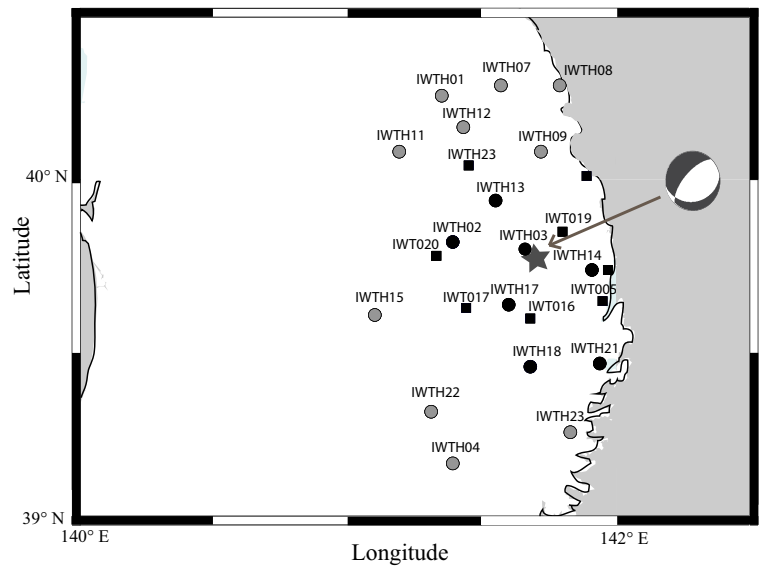
$\sigma_k = 0$. In the forward dynamic model, rupture starts at the hypocenter, triggered by a small circular asperity. Once the rupture breaks the small asperity, it will grow or stop spontaneously depending on the values of the stress field σ_0 and the friction law. For the dynamic inversion, Ruiz and Madariaga (2013) used a total of 10 parameters, which included the parameters of the friction law and the geometry of the fault. The initial asperity may be located anywhere inside the fault. Its location was part of the inversion. Since from seismic data we cannot distinguish between the barrier and asperity models (Ruiz and Madariaga 2011), the inversion was made using the asperity model; the region outside the ellipse was considered to have a very large negative initial stress load that was enough to stop the rupture when it reached the edge of the ellipse. Converting an asperity model into a barrier model is straightforward. The synthetic and observed records were compared using a simple normalized L2 norm. The search for the best model was made using the neighborhood algorithm (NA) of Sambridge (1999, 2001) although other minimization techniques, such as a genetic algorithm, can be used (Diaz-Mojica et al. 2014).

A three-dimensional fourth-order staggered-grid finite difference method with absorbing boundaries and thin fault boundary conditions was used to solve the forward dynamic rupture simulation (Madariaga et al. 1998; Dalguer and Day 2007). The spatial and temporal steps were 200 m and 0.005 s respectively, so that the CFL constant ($H = \beta \Delta t / \Delta x$) for this grid is everywhere

less than 0.3 and the finite difference method is stable. The grid had $160 \times 160 \times 160$ elements and was centered at the hypocenter on the fault plane. The fault zone was 32-km wide and 32-km deep but only a small part broke during the earthquake. The AXITRA spectral code was used to simulate wave propagation from the source to the receivers (Coutant 1990). For AXITRA, we used a velocity model proposed by Suzuki et al. (2009). For the dynamic modeling with finite differences, the structure near the source was assumed to be homogeneous with shear wave speed 4.45 km/s, density of 3300 kg/m^3, and a rigidity of 66 GPa.

Non-linear dynamic inversion was carried out for the strong motion records located within a 40-km radius from the epicenter. Beyond this distance, conversion into local surface waves may affect the records significantly. Table 1 shows the optimal values for the most significant parameters obtained by dynamic inversion. In the table, a and b are the semiaxes of the source ellipse and the stresses are referred to kinematic friction $\sigma_k = 0$. The best model obtained by the neighborhood algorithm had a misfit $\chi_2 = 0.4$, meaning that our model explains 60 % of the observed data, which also converge to a seismic moment M_0 1.5×10^{19} Nm, similar to that

Table 1 Parameters for the best model inverted for the 2008 Iwate earthquake

a (km)	b (km)	σ_s (MPa)	σ_s (MPa)	D_c (m)
4.02	8.06	34.25	55.96	1
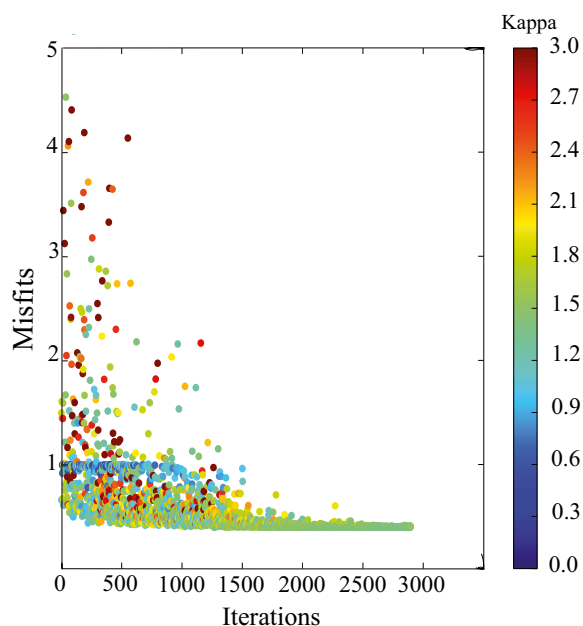
Fig. 9 Convergence of the neighborhood algorithm misfit with iteration for the dynamic inversion of the 2008 Iwate earthquake. A total of 3000 models were tested until convergence was obtained (Ruiz and Madariaga 2013)

obtained by Suzuki et al. (2009) from kinematic inversion.

The misfits for each step in the inversion are shown in Fig. 9. In this figure, we also show the values of κ computed according to Eq. 21 for each model using an average radius of the source ellipse for R; k converges to the value 1.34. The convergence to a well-defined value of k can be explained by a tradeoff between the initial stress and the friction law parameters.

Figure 10 shows snapshots of the slip rate on the fault plotted every 0.4 s. The largest values of slip rate are attained near the boundaries of the ellipse where the large negative stress stopped the rupture. The overall characteristics are short rupture duration of less than 2.1 s, implying a very high sub-shear rupture velocity. Rupture starts in the small asperity and then propagates to the rest of the fault, mainly in a direction away from the surface. The overall slip distribution for our dynamic model is a simplified version of the kinematic slip distribution obtained by Suzuki et al. (2009). Overall size and moment are the same although the kinematic slip distribution is heterogeneous with a main slip patch similar to ours.

The results listed in Table 1 and shown in the preceding figures indicate that the Iwate intermediate-depth

earthquake had a relatively small size considering that the maximum slip was 4 m. The moment of the event was $1.5 \, 10^{19}$ Nm. As a consequence, the stress drop was large, 34.7 MPa. The most important parameters from a dynamic point of view are the peak friction stress $\sigma_s = 56$ MPa and the slip-weakening distance $D_c = 1$ m, which together give an energy release rate of 23 MJ/m^2; this is also very large compared with those estimated for events of this magnitude at shallower depths. This result may not be generalized to other intermediate-depth earthquakes because, as show by Allmann and Shearer (2009), stress drops determined from spectral analysis vary widely in different geographical zones and stress regimes. See also Vallee (2013) who reported that shallow and deep events have similar strain drops at shallow and intermediate depths, stress drops increasing only due to the increase of rigidity.

The synthetic displacements reproduce the observed records very well. Figure 11a shows the simulation of the EW components of stations iwth03 and inth23. The synthetics and observed records have not been corrected for any time shift so that the velocity model and the structure at the source are compatible. The duration of the signals is of the order of 4–5 s, implying a very fast rupture and a massive stress drop. In Fig. 11b, we also show the Fourier spectra computed for the two records shown in Fig. 11a. The dynamic models fit the spectra very well: they all resemble Brune's ω^{-2} model below the low-frequency cutoff of the low-pass filter applied to the data.

5.2 Resolution of the inverse problem

Whether one uses kinematic or dynamic inversion, a crucial test of the inversion is the non-uniqueness of the solutions. In order to test this point, we proceeded to do a large number of models using a variation of the classical Monte Carlo technique. For this purpose, we chose a small subset of the parameter space to explore values of the dynamic parameters σ_0, σ_s, and D_c, keeping all other parameters fixed to those of the best model obtained using NA, Table 1. In Fig. 12, we plot the results of Monte Carlo exploration. Models with misfits lower than 0.5 are drawn with large dots, larger misfits are saturated to 0.5. These large dots represent a family of models that fit the observations well. Figure 12a show the seismic moment M_0 of the models against their k. All the models that fit the data with error less than 50 % are grouped in an area where the seismic moment varies

Fig. 10 Snapshots of the slip rate field for at 0.4-s intervals for the best model found by dynamic inversion for the 2008 Iwate earthquake (Ruiz and Madariaga 2013). The sides of each square are 32 km in length
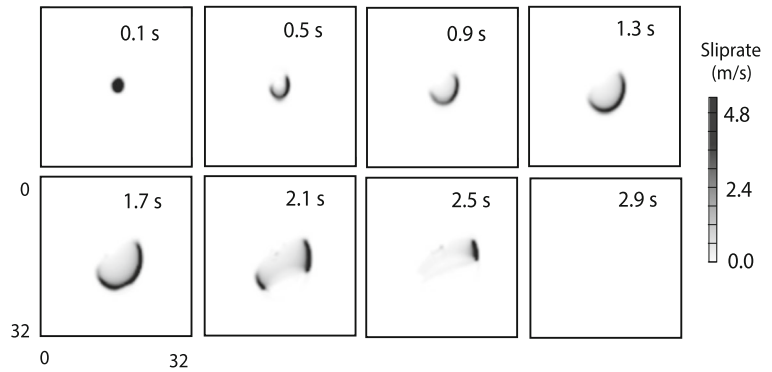

around 1.5×10^{19} Nm and k varies between 1 and 1.5. Figure 12b shows the relation among S, k, and the misfits of all models. We observe that the acceptable solutions are located in an intersection of k and S values. Then, k and S are parameters that control rupture propagation better than σ_0, σ_s, and D_c, independently.

6 Discussion and Conclusions

We have reviewed the development of earthquake dynamics of circular faults from a relatively simple subject whose main purpose was to explain the origin of seismic radiation and establish general scaling relations between seismic radiation, seismic moment, and the size of earthquakes. It was soon realized that ruptures were controlled by the relative values of stress drop and the friction law that opposes slip between the two sides of the fault. Curiously, although very complex models of faulting have been proposed including the role of many mechanical properties like advanced friction laws, pore pressure effects, thermal effects, etc., the study of earthquake radiation by the propagation of rupture has been relatively limited. A possible explanation is that it is not obvious how those complexities affect seismic radiation and how much of it is observable. As shown by Madariaga (1977) and many others, the radiation of seismic waves into the far field is largely dominated by large changes in the propagation speed and stress conditions near the rupture front rather than the conditions under which ruptures propagate. Actually, one of the curious results of early studies in dynamics is that a rupture front moving at constant speed does not radiate. This was established very early in the study of earthquake dynamics in a series of papers published in the early 1970s by Freund (1972a, b) and Kostrov

Fig. 11 The observed and synthetic seismograms and spectra for two stations that recorded the 2008 Iwate earthquake. Station IWTH03 was located close to the epicenter and IWTH23 was some 50 km to the south
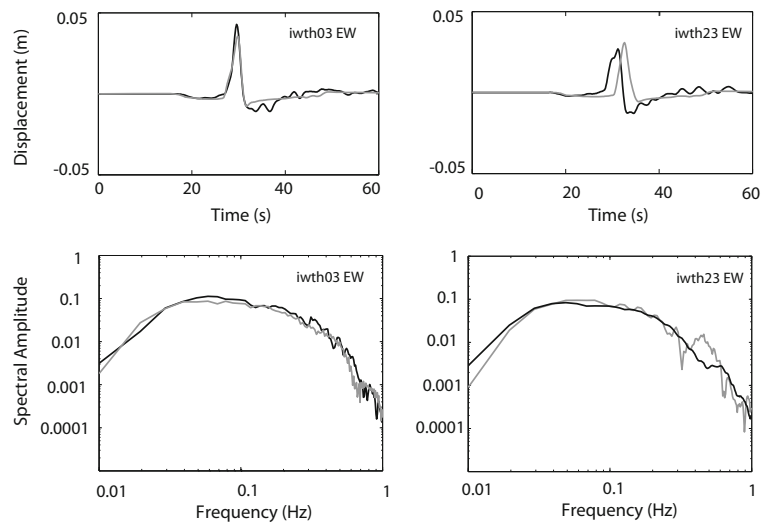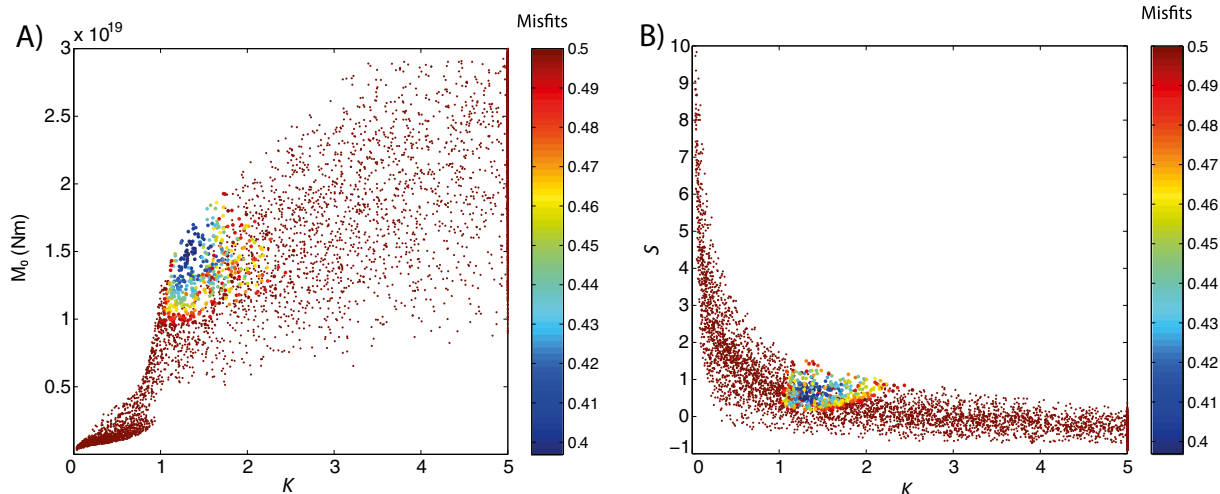
Fig. 12 Study of the resolution of the dynamic inversion. Each *dot* is colored by the misfit value following the color scale shown on the right. The scale is saturated for misfits ≥0.5. Better models (*blue*) occupy a limited zone of the parameter-moment space. **a** Projection of model space onto the plane M_0, κ. The misfits lower

than 0.5 are controlled by the seismic moment (M_0 1.5×10^{19} Nm) and a narrow band of κ values (1:1.5). **b** Projection of model space onto the plane S, κ, the solutions with low misfits are grouped again in a small area.

(1966, 1973) and later generalized by Madariaga (1983) for an arbitrarily moving rupture in antiplane mode.

Earthquake dynamics was initially based on the solution of a relatively simple, but well-defined problem: the rupture of a circular crack by a rupture that started at the center of the fault and propagated at constant speed (Kostrov 1964). This model has a high degree of symmetry, but in spite of this, its solution is not symmetric as a consequence of the different response of the earth to modes II and III type of fracture. Radiation from this model is quite complex; but for most practical applications, it is often reduced to a single spectral shape of the ω^{-2} type proposed by Aki (1967) and Brune (1970). The advantage of the simple crack model is that the energy balance can be established completely, i.e., strain energy, radiated energy, and fracture energy are known. Since fracture energy release depends on the speed of the rupture front, rupture velocity plays a major role in the energy balance. This is the reason that radiated energy and moment scale differently (see Ide and Beroza 2001). Apparent stress or energy moment ratio is not the same for all earthquakes producing departure from strict static self-similarity. The simple quasi-dynamic rupture model has been extended to a more natural spontaneous rupture model by many authors starting with Day (1982). Recently, Kaneko and Shearer (2014, 2015) have done extensive analysis of the problem for many spontaneous circular and elliptical rupture. The variation of corner frequency

around the source is quite large as could be expected from simple energetic arguments.

Another approach to earthquake dynamics that remains still difficult in practice is dynamic inversion, i.e., directly searching for the rupture model from seismic observations. The main problem is the cost of numerical modeling of the rupture process, but the modeling is very rapidly becoming possible at least for events that occur in places where local site effects do not affect ground motion very seriously. The main issue in dynamic inversion is the parameterization of the source and its rupture process. Most seismologists and geodesists are used to linearization; this is achieved by dividing the source into small rectangles of uniform slip. This method is not easy to apply to dynamic models where most of the information comes from the borders of the rupture and from internal asperities. These are very non-linearly related to the seismic waves emitted by the earthquake. In spite of these difficulties, we showed that it is possible with present day resources to do limited non-linear inversion for seismic sources in the single elliptical approximation. This should improve as better seismic observations become available and improvements in seismic wave simulation open the way to large inversions.

References

Abercombrie RE, Rice JR (2005) Can observations of earthquake scaling constrain slip weakening? Geophys J Int 162:406–424

Aki K (1967) Scaling law of seismic spectrum. J Geophys Res 73:5359–5376

Allmann BP, Shearer PM (2009) Global variations of stress drop for moderate to large earthquakes. J Geophys Res 114, B01310. doi:10.1029/2008JB005821

Andrews DJ (1976) Rupture velocity of plain stress shear cracks. J Geophys Res 81:5679–5687

Ben-Menahem A (1962) Radiation of seismic body waves from finite moving sources in the earth. J Geophys Res 67:396–474

Ben-Menahem A, Harkrider DG (1964) Radiation patterns of seismic surface waves from buried dipolar point sources in a flat stratified earth. J Geophys Res 69:2605–2620

Bizzarri A, Cocco M (2003) Slip-weakening behavior during the propagation of dynamic ruptures obeying rate- and state-dependent friction laws. J Geophys Res 108. doi: 10.1029/2002JB002198

Bouchon M (1997) The state of stress on some faults of the San Andreas system as inferred from near-field strong motion data. J Geophys Res 102:1731–1744

Brune J (1970) Tectonic stress and the spectra of seismic shear waves from earthquakes. J Geophys Res 75:4997–5009

Brune J (1971) Correction J Geophys Res 76:5002

Burridge R, Halliday GS (1977) Dynamic shear cracks with friction as models for shallow focus earthquakes. Geophys J Roy Astr Soc 25:261–283

Corish SC, Bradley R, Olsen KB (2007) Assessment of a nonlinear dynamic rupture inversion technique. Bull Seismol Soc Am 97:901–914

Coutant O (1990) Programme de simulation numerique AXITRA, Rapport LGIT. Univ. Joseph Fourier, Grenoble

Dalguer LA, Day SM (2007) Staggered-grid split-node method for spontaneous rupture simulation. J Geophys Res 112:B02302, doi:10.101029/2006JB004467

Das S (1980) A numerical method for determination of source time functions for general 3 dimensional rupture propagation. Geophys J Roy Astr Soc 62:591–604

Das S, Aki K (1977) A numerical study of two dimensional spontaneous rupture propagation. Geophys J Roy Astr Soc 50:643–668

Daub EG, Carlson JM (2008) A constitutive model for fault gouge deformation in dynamic rupture simulations. J Geophys Res 113, B12309. doi:10.1029/2007JB005377

Day S (1982) Three dimensional simulation of spontaneous rupture, the effect of non uniform prestress. Bull Seism Soc Am 72:1881–1902

Di Carli S, Francois-Holden C, Peyrat S, Madariaga R (2010) Dynamic inversion of the 2000 Tottori earthquake based on elliptical subfault approximations. J Geophys Res 115(B12): 328. doi:10.1029/2009JB006358

Diaz-Mojica J, Cruz-Atienza VM, Madariaga R, Singh SK, Tago J., Iglesias A (2014) Dynamic source inversion of the M6.5 intermediate depth Zumpango earthquake in central Mexico: A parallel genetic algorithm. J Geophys Res 119. doi:10.1002/2013JB010854

Eshelby JD (1957) The determination of the elastic field of an ellipsoidal inclusion and related problems. Proc Roy Soc A 241:376–396

Eshelby JD (1959) The elastic field outside an ellipsoidal inclusion. Proc Royal Soc A 252:561–569

Freund LB (1972a) Crack propagation in an elastic solid subjected to general loading - I. Constant rate of extension. J Mech Phys Solids 20:129–140

Freund LB (1972b) Energy flux into the tip of an extending crack in an elastic solid. J Elasticity 2:341–349

Fukuyama E, Mikumo T (1993) Dynamic rupture analysis: inversion for the source process of the 1990 Izu-Oshima, Japan, earthquake (M = 6.5). J Geophys Res 98:2156–2202

Griffith A (1921) The phenomenon of rupture and flow in fluids. Phil Trans Roy Soc 221:163–198

Hanks TC (1977) Earthquake stress-drops, ambient tectonics stresses and stresses that drive plates. Pure Appl Geophysics 115:441–458

Haskell NA (1964) Total energy and energy spectral density of elastic wave radiation from propagating faults. Bull Seism Soc Am 54:1811–1841

Haskell NA (1966) Total energy and energy spectral density of elastic wave radiation from propagating faults, Part II. Bull Seism Soc Am 56:125–140

Husseini MI, Randall MJ (1976) Rupture velocity and radiation efficiency. Bull Seism Soc Am 66:1173–1187

Ida Y (1972) Cohesive forces across the tip of a longitudinal shear crack and Griffith's specific surface energy. J Geophys Res 77:3796–3805

Ide S (2002) Estimation of radiated energy of finite-source earthquake models. Bull Seism Soc Am 92:2994–3005

Ide S, Beroza GC (2001) Does apparent stress vary with earthquake size? Geophys Res Lett 28:3349–3352

Ide S, Takeo M (1997) Determination of constitutive relations of fault slip based on seismic wave analysis. J Geophys Res 102, 27:379–27 391

Kanamori H, Anderson DL (1975) Theoretical basis of some empirical relations in seismology. Bull Seism Soc Am 65:1073–1095

Kaneko Y, Shearer PM (2014) Seismic source spectra and estimated stress drop derived from cohesive-zone models of circular subshear rupture. Geophys J Int 197:1002–1015

Kaneko Y, Shearer PM (2015) Variability of seismic source spectra, estimated stress drop, and radiated energy, derived from cohesive-zone models of symmetrical and asymmetrical circular and elliptical ruptures. J Geophys Res 120(2):1053–1079. doi:10.1002/2014JB011642

Keylis-Borok BV (1959) On the estimation of the displacement in an earthquake source and of source dimensions. Ann Geofisica 12:205–214

Kostrov BV (1964) Self-similar problems of propagation of shear cracks. J Appl Math Mech 28:1077–1087

Kostrov BV (1966) Unsteady propagation of longitudinal cracks. J Appl Math Mech 30:1241–1248

Kostrov BV (1975) On the crack propagation with variable velocity. Int J Fracture 11:47–56

Lancieri M, Madariaga R, Bonilla F (2012) Spectral scaling of the aftershocks of the Tocopilla 2007 earthquake in northern Chile. Geophys J Int 188:469–480

Madariaga R (1976) Dynamics of an expanding circular fault. Bull Seism Soc Am 66:639–666

Madariaga R (1977) High frequency radiation from crack (stress drop) models of earthquake faulting. Geophys J Roy Astr Soc 51:525–651

Madariaga R (1983) High frequency radiation from dynamic earthquake fault models. Ann Geophys 1:17–23

Madariaga R, Olsen KB (2002) Earthquake dynamics. Int Handbook of Earthquake and Engineering Seismology 81A:175–194

Madariaga R, Olsen KB, Archuleta R (1998) Modeling dynamic rupture in a 3D earthquake fault model. Bull Seism Soc Am 88:1182–1197

Palmer AC, Rice JR (1973) The growth of slip surfaces in the progressive failure of over-consolidated clay. Proc Roy Soc A 332:527–548

Peyrat S, Olsen KB (2004) Nonlinear dynamic rupture inversion of the 2000 Western Tottori, Japan, earthquake.. doi:10.1029/2003GL019058

Peyrat S, Olsen KB, Madariaga R (2001) Dynamic modeling of the 1992 Landers earthquake. J Geophys Res 106(26):467–482

Rice JR (1968) A path-independent integral and the approximate analysis of strain concentration by notches and bars. J App Mechanics 35:379–386

Ruiz S, Madariaga R (2011) Determination of the friction law parameters of the Mw 6.7 Michilla earthquake in northern Chile by dynamic inversion. Geophys Res Lett 38, L09317. doi:10.1029/2011GL047147

Ruiz S, Madariaga R (2013) Kinematic and dynamic inversion of the 2008 Northern Iwate earthquake. Bull Seism Soc Am 103:694–708

Sambridge M (1999) Geophysical inversion with a Neighbourhood Algorithm – I. Searching a parameter space. Geophys J Int 138:479–494

Sambridge M (2001) Finding acceptable models in nonlinear inverse problems using a neighbourhood algorithm. Inverse Problems 17:387–403

Sato T, Hirasawa T (1973) Body wave spectra from propagating shear cracks. J Phys Earth 21:415–431

Suzuki W, Aoi S, Sekiguchi H (2009) Rupture process of the 2008 northern Iwate intraslab earthquake derived from strong-motion records. Bull Seism Soc Am 99:2825–2835

Twardzik C, Das S, Madariaga R (2014) Inversion for the physical parameters that control the source dynamics of the 2004 Parkfield earthquake. J Geophys Res 119. doi:10.1002/2014JB011238

Udias A, Madariaga R, Buforn E (2013) Source mechanisms of earthquakes theory and practice. Cambridge University Press, Cambridge

Vallee M (2013) Source time function properties indicate a strain drop independent of earthquake depth and magnitude. Nat Commun 4:2606. doi:10.1038/ncomms3606

Vallée M, Bouchon M (2004) Imaging coseismic rupture in far field by slip patches. Geophys J Int 156:615–630

Zollo A, Emolo A (2011) Terremoti e Onde (in Italian). Liguore Editori, Napoli